Check for updates

An aeromagnetic denoising-decomposition-3D inversion approach for mineral exploration

Min Ma[1,2,3], Liancun Xiu[1], Qi Gao[3], Yongli Li[3], Wenjie Wang[3], Haoqing Xu[3] and Wenhui Zhou[3]*

[1]Chinese Academy of Geological Sciences, Beijing, China, [2]School of Earth Sciences and Resources, China University of Geosciences, Beijing, China, [3]Hohhot General Survey of Natural Resources Center, China Geological Survey, Hohhot, China

Reduction of aeromagnetic noise and extraction of mineralization-related residual anomalies are critical for aeromagnetic data processing in mineral exploration. This study introduced a multifractal singular value decomposition (MSVD) method to remove the noise and improved the bi-dimensional empirical mode decomposition (BEMD) algorithm to extract residual magnetic anomalies. It is shown that MSVD and improved BEMD could effectively reduce the noise and extract residual magnetic anomalies. Then, a wavenumber−domain iterative approach is applied in 3D imaging of magnetic anomalies and gradients with depth constraints, which is a rapid tool for qualitative and quantitative interpretation of magnetic data and is suitable for rapidly imaging large-scale data. The 3D inversion result is verified by four geological sections along the regional tectonic directions and some drilling holes on the deposits. It is revealed that this proposed approach is practical and effective in dealing with aeromagnetic data interpretation and inversion for mineral exploration.
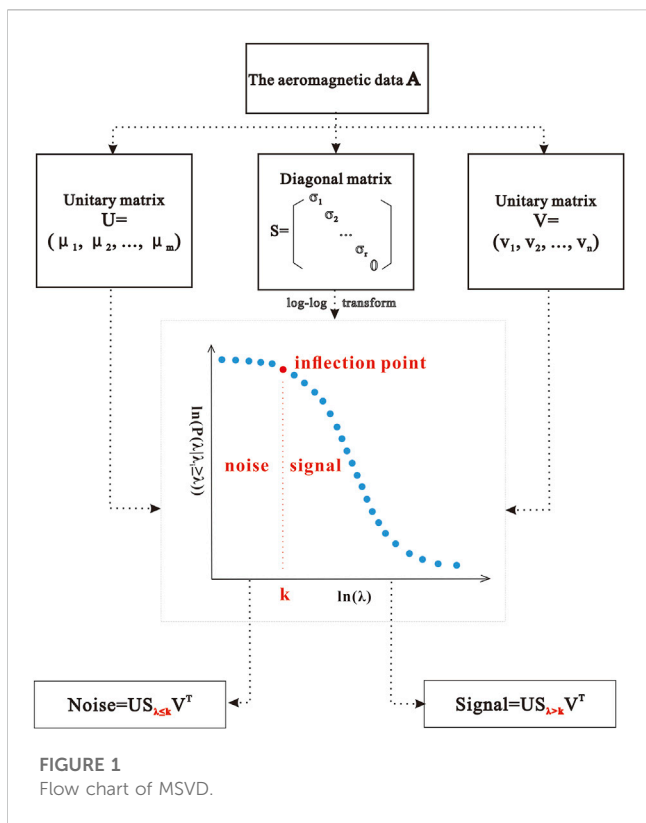
KEYWORDS

aeromagnetic denoising, MSVD, residual anomaly extraction, improved BEMD, 3D inversion, mineral exploration

1 Introduction

Aeromagnetic exploration is a powerful and fast, convenient and economical technique enabling the delineation of geological structures and exploration of mineral resources. It has been applied in the exploration of geotectonics, faults, igneous rocks, craters, magnetic-related polymetallic deposits, and extraction of hydrothermal alterations (Muundjua et al., 2007; Ortiz-Alemán and Urrutia-Fucugauchi, 2010; Gao et al., 2016; Elkhateeb and Abdellatif, 2018; Sridhar et al., 2018; Eldosouky et al., 2020; Shebl et al., 2021; Xiong, 2021; Bencharef et al., 2022; Ekpe et al., 2022; ElGalladi et al., 2022; Mahdi et al., 2022; Mamouch et al., 2023). Hereinto, two factors have to be taken into account before interpretation or inversion.

The first one is the noise in the aeromagnetic data, which is usually random or fringe-pattern alike. The noise could be generated not only by the ground objects such as the power transmission lines and transmission substations but also by the ferromagnet in the aircraft itself. In addition, the differences between the aircraft

FIGURE 1
Flow chart of MSVD.

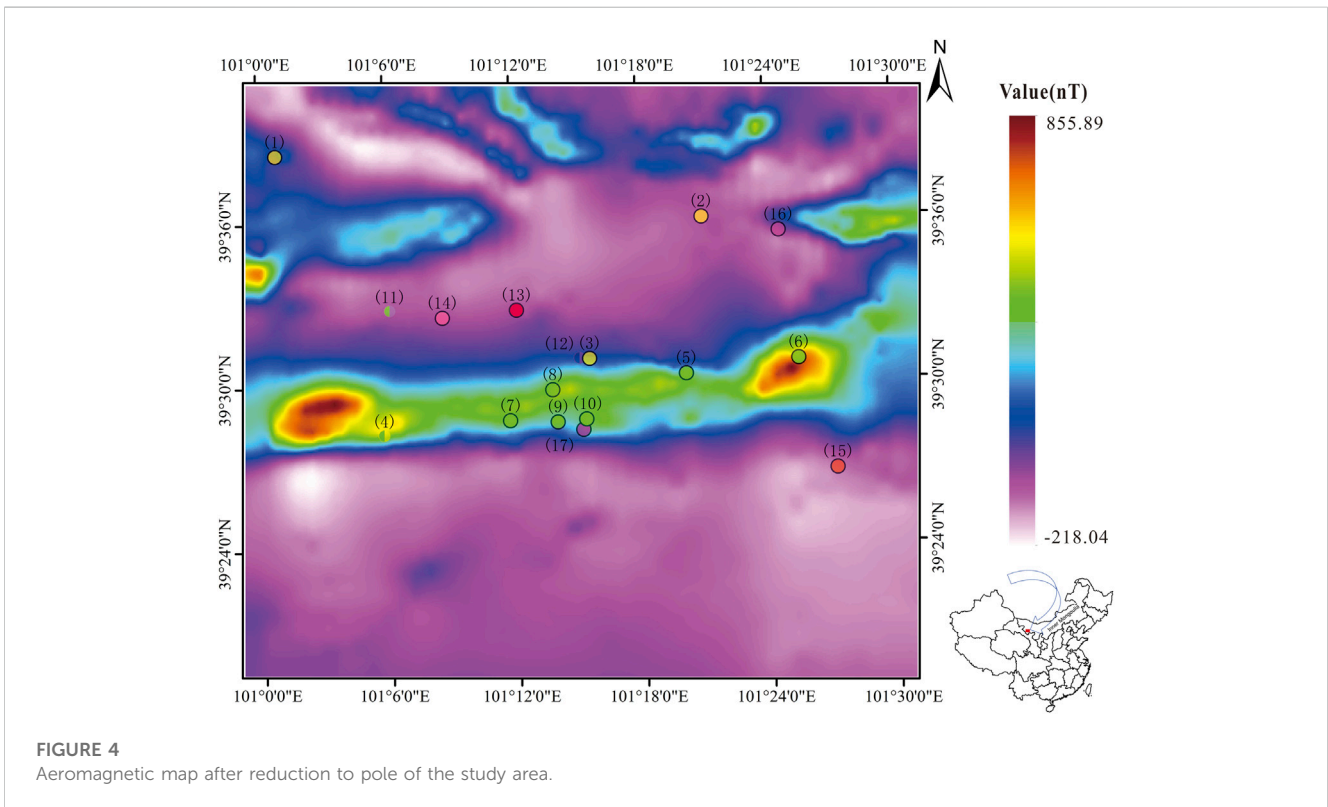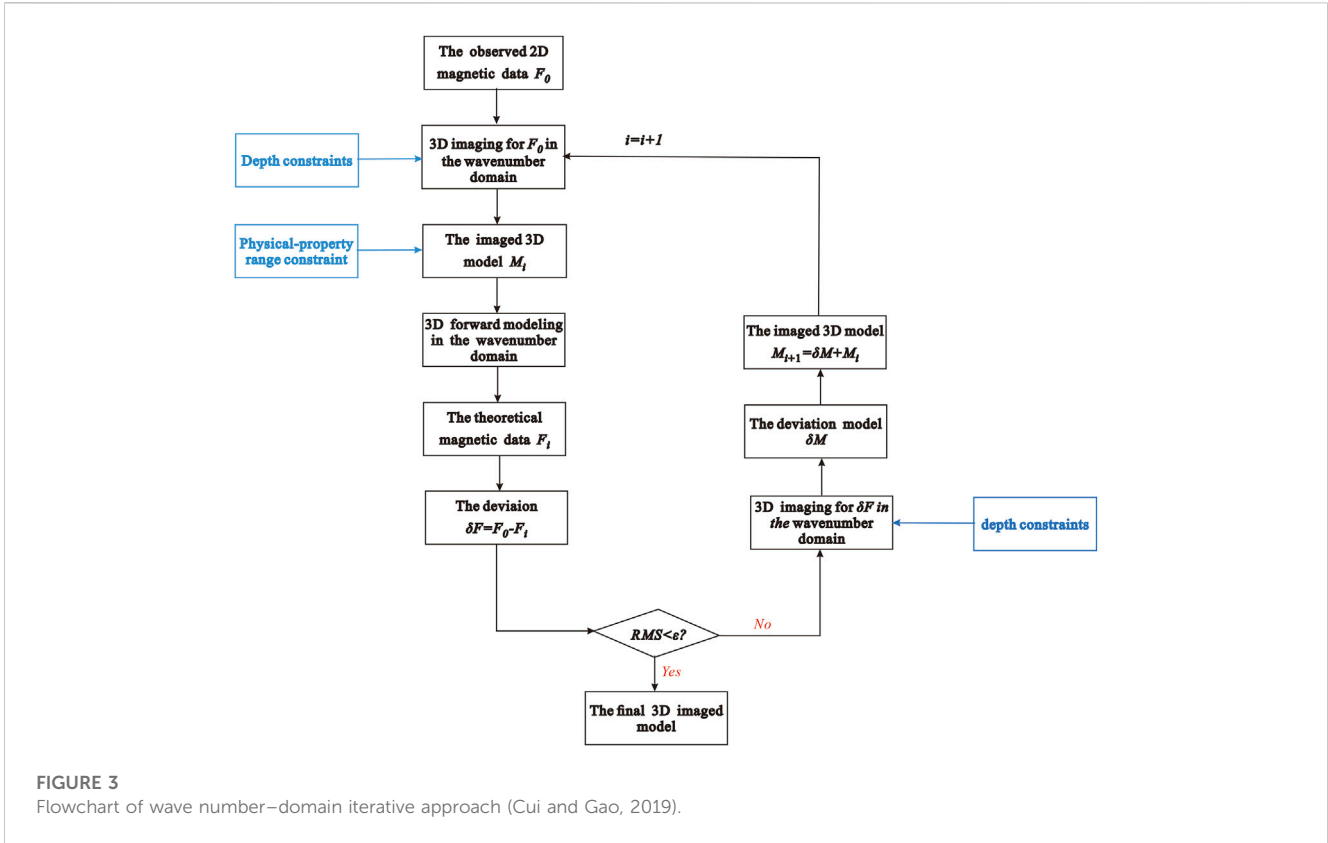airlines and the processing of reduction to the magnetic pole could also cause fringe-pattern noise aligned along the declination direction (Li and Nabighian, 2015). The noise is usually very small in quantity but will make the aeromagnetic data artificial and aliasing (Ma et al., 2019). The commonly used denoising methods are mainly focused on low-pass filter algorithms like moving average (Liu et al., 2015), Wiener filter (Lee and Lee, 2021), maximum likelihood filter (Bouhrara et al., 2019), and wavelet transform (Lin et al., 2022). The method of upward continuation to a certain height (Zhu and Lu, 2021; Tazi et al., 2022; Zhu et al., 2022) could also suppress

the noise to some extent while enhancing the deep anomalies. However, the drawback of a low-pass filter is that it will filter out some useful high-frequency information while denoising. Fortunately, the method of MSVD (multiscale or multi-fractal singular value decomposition) is especially sensitive to noise and is practical in denoising when the noise level is low (Di Pietro Paolo et al., 2006; Little et al., 2017). It could decompose the aeromagnetic data into a series of singular values from high to low frequencies, in which the high-frequency noise could be separated by selecting the corresponding singular values and usually without filtering out the useful high-frequency information. The second one is anomaly separation or extraction of residual anomalies. Separation of regional and residual aeromagnetic anomalies is considered very essential before any qualitative and quantitative interpretation process. The reason is that the observed aeromagnetic anomalies represent the combined effects of sources under different depth, density, or magnetic variation, especially for metallic deposits (Abdelrahman and Sharafeldin, 1996; Al-Rahim, 2016; Zahra and Nakhla, 2016). What really needs to be inversed is the mineralization-targeted or residual anomalies after removing the regional (background) anomalies and the neighboring interferences. There are some filtering techniques that have been applied to deal with this regional–residual separation issue, such as graphical separation (Gupta and Ramani, 1980), radial power spectrum analysis (Zahra and Nakhla, 2016; Elkhateeb and Abdellatif, 2018), match filter (Spector and Grant, 1970), preferential filtering method (Guo et al., 2013), polynomial fitting (Martínez-Moreno et al., 2015; Gabtni and Jallouli, 2017; Innocent et al., 2019), fast Fourier transform (Saada et al., 2022), and upward continuation (Eldosouky et al., 2022). However, there are no unique and absolute solutions for regional–residual anomaly separation. Some of the separation techniques are not suitable for handling data characterized by both the non-linear and non-stationary nature (Mandal and Niyogi, 2018). All separation techniques hypothesize about source distribution. The general assumption is that the observed

FIGURE 2
Schematic diagram of the improved BEMD algorithm.

FIGURE 3
Flowchart of wave number−domain iterative approach (Cui and Gao, 2019).

FIGURE 4
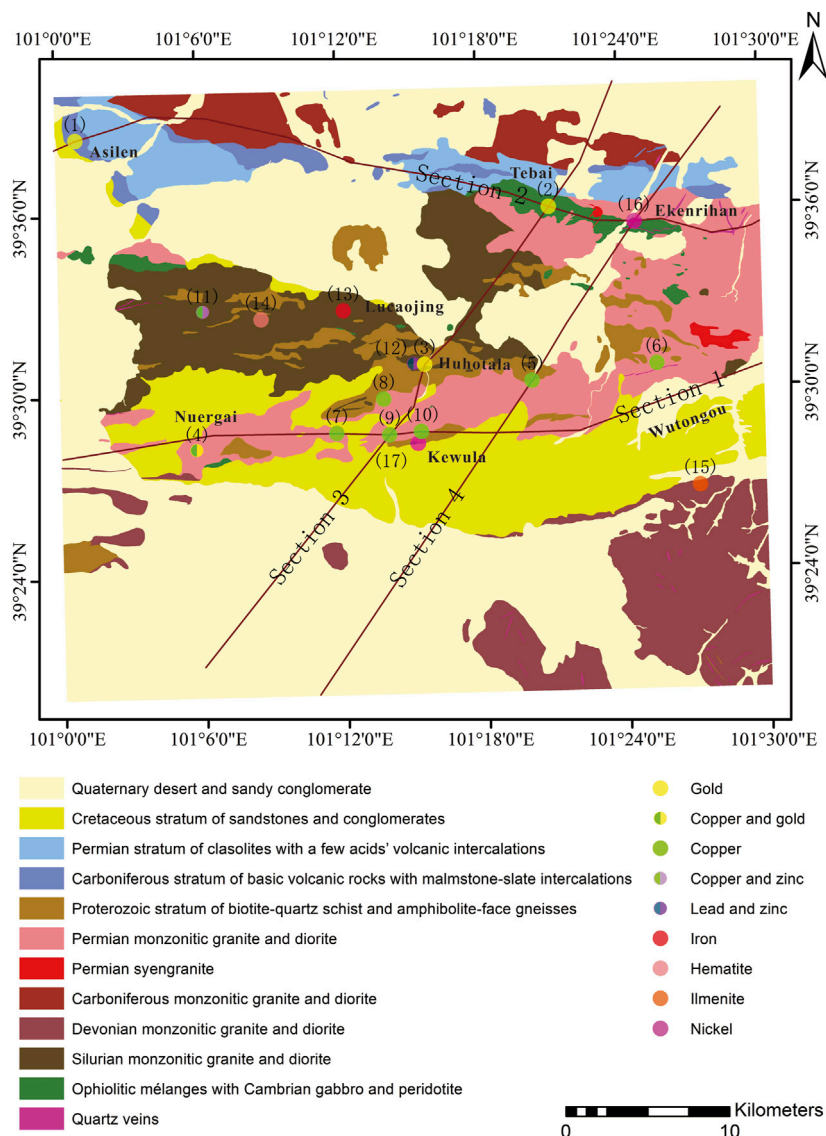Aeromagnetic map after reduction to pole of the study area.

FIGURE 5
Geological mapping of the study area.

field is the sum of the effect of shallow and deep sources (Keating and Pinet, 2011). Fortunately, BEMD (bi-dimensional empirical mode decomposition) is an additive, independent, and self-adaptive algorithm that could exactly separate the anomalies into different components from the high-pass to the low-pass, showing the anomalies from the local to the regional scale. The best factor of all is that the original magnetic field is the summation of the decomposed components called BIMFs (bi-dimensional intrinsic mode functions). Some improvements of this algorithm are made in this study by ordinary kriging interpolation and self-adaptive sifting process to overcome its mode mixing problem. After removing the noise and regional anomalies, the mineralization-related residual anomalies could be embodied for 3D inversion. The Euler deconvolution

method, tilt depth method, and 3D inversion by Geosoft's VOXI Earth Modeling are commonly used methods in tracing the position and depth of the origins of magnetic anomalies and estimating the 3D magnetic susceptibility distribution (Eldosouky et al., 2021; Kharbish et al., 2022). In this study, a method of wavenumber-domain iterative approach for 3D imaging of magnetic anomalies and gradients with depth constraints is applied for 3D inversion, which is especially suitable for rapidly imaging large-scale data and for showing the 3D magnetic susceptibility distribution volumetrically (Cui and Guo, 2019).

The paper is organized as follows: Section 1 introduces the approach. Section 2 explains the principles of MSVD and improvements of BEMD and makes a brief introduction of MagFInv3D for inversion. Section 3 applies the approach to

denoising, regional–residual anomaly separation, and 3D inversion and delineates the results. Section 4 validates the result by verification of four geology sections that are regional faults along the tectonic directions and by revelation of some drilling holes, and compares the proposed MSVD-BEMD-MagFInv3D approach and directly applying MagFInv3D for inversion without removing the noise and the regional anomalies. At last, Section 5 gives some conclusions. The algorithms are programmed by MATLAB 2022b.

2 Methodology

2.1 Denoising by multifractal singular value decomposition (MSVD)

The aeromagnetic data A can be decomposed into a unitary matrix U, a diagonal matrix S with $\sigma_i = \sqrt{\lambda_i}$ (i=1, 2, 3...r) as its singular value and r as its rank, and a unitary matrix V in Eq. 1; Figure 1. The singular values correspond to the spectral energy densities, which represent a fractal or multifractal distribution described by a power law function (Cheng, 2005; Zhao and Chen, 2011; Wang et al., 2012). It does not need to estimate the power spectrum, so there are no map edge effects by MSVD (Cheng et al., 2000). The singular values of σ_i in matrix S are distributed in decreasing order along its main diagonal. They can be automatically fitted into a number of straight lines according to the inflection points where the fitting errors of all lines reach minimum synchronously on these locations. Each line represents a certain kind of noise or signal. Different kinds of aeromagnetic noise can be constructed and subtracted from the original aeromagnetic data in this way, and the signal can be rebuilt by these singular values.

$$A = U_{m\times m}S_{m\times n}V_{n\times n}^T = U_{m\times m}\begin{pmatrix} D_{r\times r} & 0 \\ 0 & 0 \end{pmatrix}V_{n\times n}^T. \quad (1)$$

2.2 Improved bi-dimensional empirical mode decomposition (improved BEMD)

The BEMD algorithm is an additive, orthogonal, self-adaptive, and multiscale decomposition method that could separate the aeromagnetic fields into different components from high to low frequencies. It has already widely been used in geochemical and geophysical anomaly mapping for these advantages (Chen et al., 2019; Zhang et al., 2020). Regional anomalies characterize geological backgrounds, and local anomalies characterize geological anomalies. As a matter of fact, some specific BIMF components that represent geological anomalies could be chosen to interpret geological features (Huang et al., 2010; Hou et al., 2012; Xu et al., 2016; Zhao et al., 2016). However, during the decomposition process, there is usually a mode mixing problem that is multifactor-induced (i.e., the noise in the data, interpolation method, and sifting process). For this reason, the improvements are made

TABLE 1 Mineral deposits in the study area.

| Deposit type	Deposit genesis
(1) Gold	Tectonic–volcanogenic
(2) Gold	Post-magmatic hydrothermal alteration-related
(3) Gold	Tectonic–hydrothermal and contact metasomatic
(4) Copper and gold	Tectonic–hydrothermal
(5) Copper	Tectonic–hydrothermal
(6) Copper	Tectonic–hydrothermal
(7) Copper	Tectonic–hydrothermal
(8) Copper	Tectonic–hydrothermal
(9) Copper	Tectonic–hydrothermal
(10) Copper	Tectonic–hydrothermal
(11) Copper and zinc	Tectonic–hydrothermal and contact metasomatic
(12) Lead and zinc	Tectonic–hydrothermal
(13) Iron	Tectonic–hydrothermal and contact metasomatic
(14) Hematite	Tectonic–hydrothermal and contact metasomatic
(15) Ilmenite	Magmatic-liquated
(16) Nickel	Magmatic-liquated
(17) Nickel	Tectonic-hydrothermal

by ordinary kriging interpolation and self-adaptive sifting processes (Ma et al., 2019). The improvement by ordinary kriging interpolation could make the BEMD algorithm converge in the decomposition process whether the original data are linear or non-linear because there are no outliers interpolated by ordinary kriging. However, other interpolation methods like RBF (radial basis function) and polynomial regression may generate outliers while interpolating in some cases. It is especially distinct while extrapolation and that may induce the mode mixing problem, and the algorithm cannot converge in this way. The improvement of the sifting process is on the condition that when the number of extrema is less than 4 or the upper–lower envelopes are colinear, then all BIMFs and a Residue are screened out. The mode mixing and excessive or incomplete decomposition could also be restrained in this way. The schematic diagram of the improved BEMD algorithm is shown in Figure 2. The aeromagnetic data set A is divided into some BIMFs and a Residue (Eq. 2), which could be grouped into a high-pass (F$_{HP}$), a band-pass (F$_{BP}$), and a low-pass (F$_{LP}$) filter (Eq. 3–5). A is the summation of these filters that are independent of one another.

$$A = \sum_{i=1}^{N} BIMF_i + Residue, \ i = 1, 2, \ldots, N. \quad (2)$$

$$F_{HP} = \sum_{i=1}^{k} BIMF_i, \ i = 1, 2, \ldots, k, \quad (3)$$

$$F_{BP} = \sum_{i=k+1}^{m} BIMF_i, \ i = k+1, k+2, \ldots, m, \quad (4)$$

$$F_{LP} = \sum_{i=m+1}^{N} BIMF_i + Residue, \ i = m+1, m+2, \ldots, N. \quad (5)$$
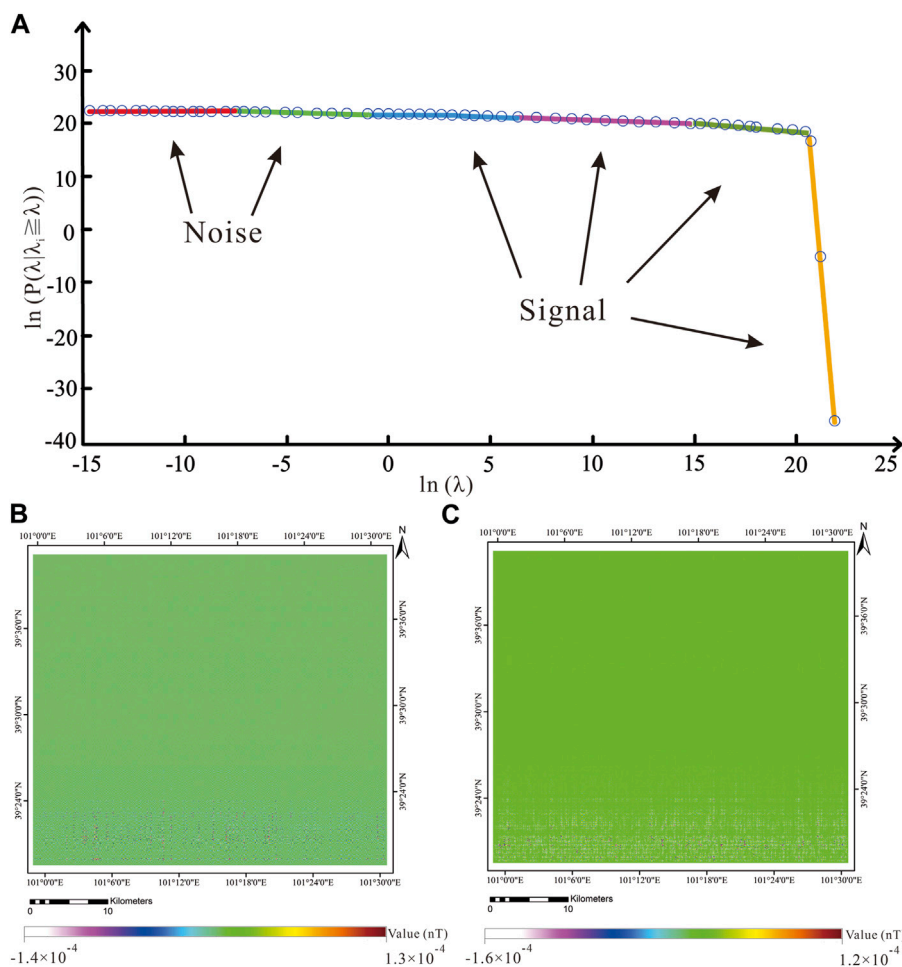
FIGURE 6
Aeromagnetic noise detection by MSVD. **(A)** Log−log transform of the singular values of the aeromagnetic data. **(B)** Noise component of the first line. **(C)** Noise component of the second line.

2.3 3D inversion by MagFInv3D

MagFInv3D is a package programmed by MATLAB, a wavenumber–domain iterative approach for 3D imaging of magnetic anomalies and gradients with depth constraints, proposed by Cui and Guo in 2019, which could be downloaded from https://github.com/earthman131/MagFInv3D. The method is especially suitable and applicable for rapidly imaging large-scale or regionally large-area-covered data. First, supposing that the underground 3D magnetic field is composed of many horizontal layers from the top to bottom, the magnetic multi-parameters (including the total magnetic anomaly, three magnetic components, magnetic gradients, and magnetic full-tensor gradients) of each horizontal layer could be calculated by applying 2D fast Fourier transform (FFT). Second, a depth-scale factor and interface constraint are applied to enhance the depth resolution. At last, the imaging accuracy is improved by iteration when the error

measured by the root mean square between the inversed theoretical magnetic data F_i and the observed magnetic data F_0 is less than the threshold ε. The flowchart of the approach is shown in Figure 3 by Cui and Guo in 2019.

3 Application and results

3.1 The study area and aeromagnetic data

The study area is in a polymetallic ore field in Inner Mongolia, northwest China, longitude [101°0′E, 101°30′E] and latitude [39°20′N, 39°40′N]. The aeromagnetic data are surveyed at a scale of 1:50,000 and processed by reduction to the magnetic pole via standardized polar transform with a declination value of −1.81° and an inclination value of 59.48°, which is shown in Figure 4 of the aeromagnetic map of the study area. Four geological sections are made along the geotectonic directions in Figure 5 of the geological mapping of the study area to
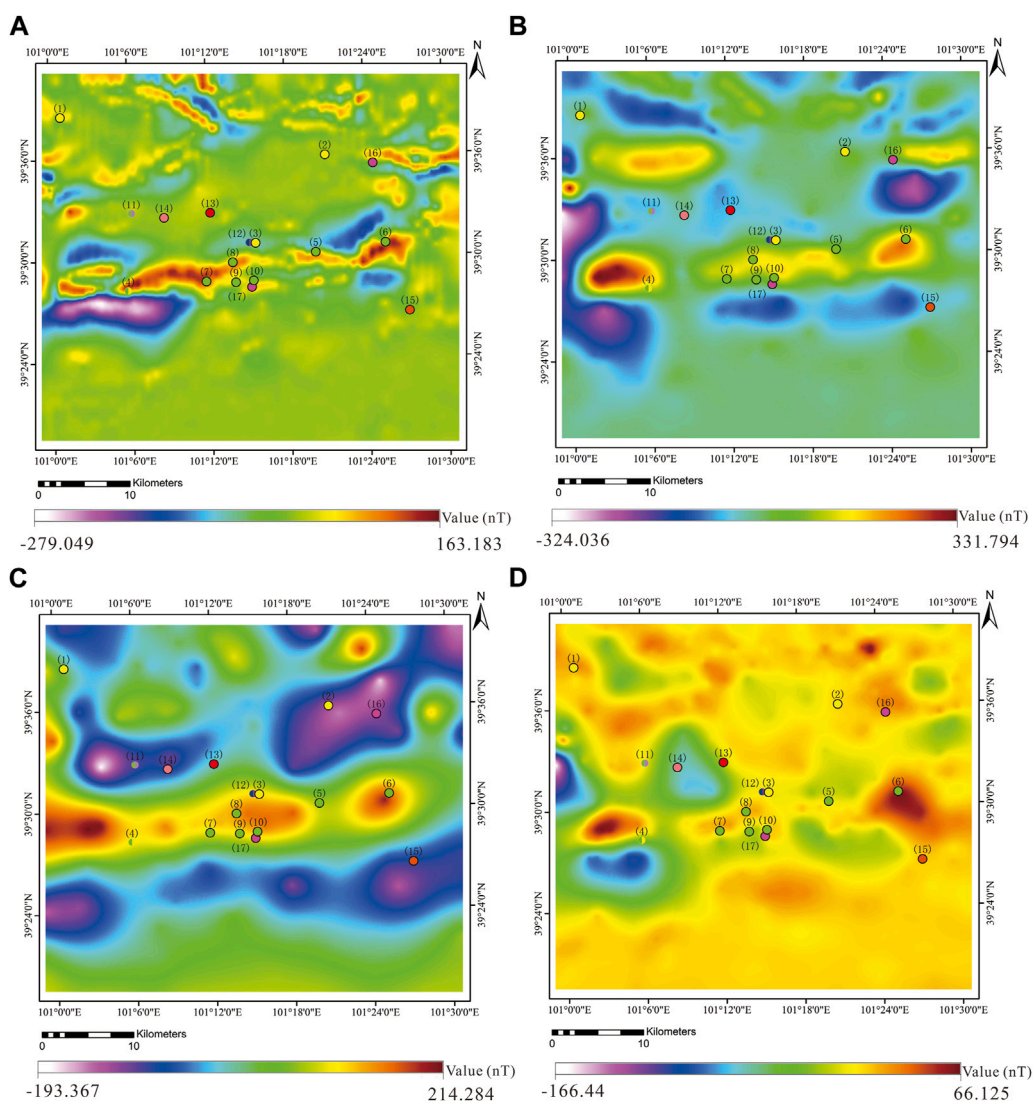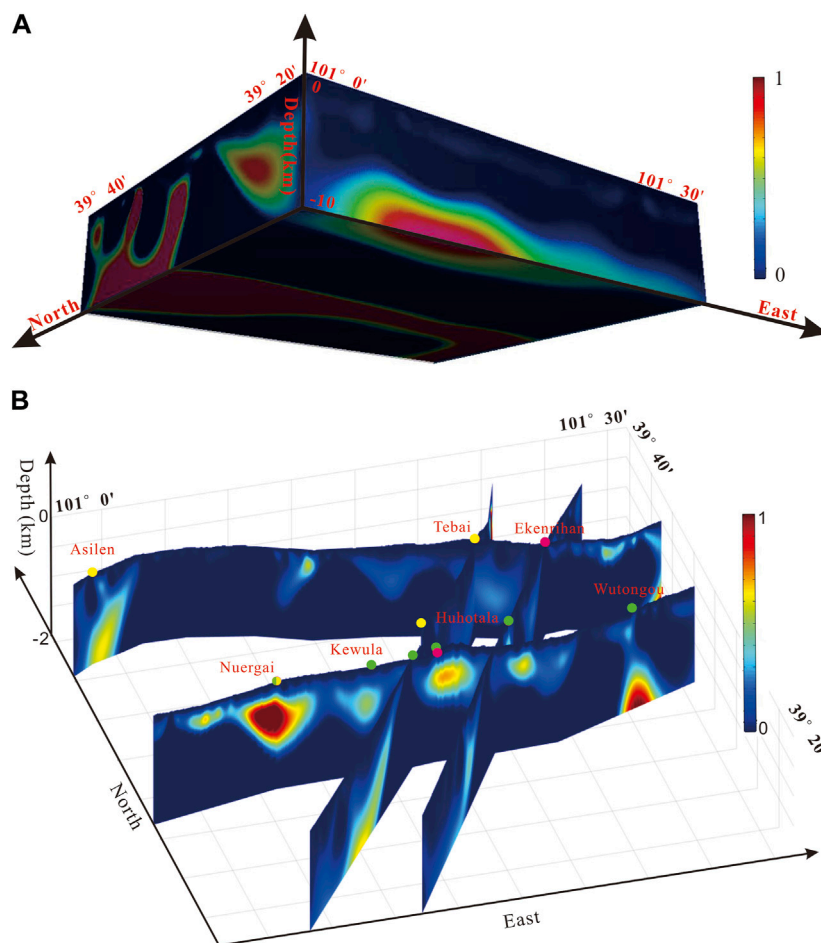
FIGURE 7
Components obtained by improved BEMD. **(A)** BIMF I, **(B)** BIMF 2, **(C)** BIMF 3, and **(D)** residue.

interpret the magnetic anomalies and are investigated at the field to delineate their geological and mineralization characteristics.

The anomalies in the study area are mainly distributed along the Nuergai–Kewula–Wutongou reverse fault along Section 1, northeast-oriented and inclined to north about 60°, which are closely related to the outcropped geological bodies along this fault (including the Proterozoic stratum that consists of biotite–quartz schist and amphibolite face gneisses, Silurian and Permian quartz diorite, and Cambrian gabbro and serpentinized peridotite). The magnetic intensity along this fault is between 50 nT and 500 nT, along which two regions with anomalies in the east and west of it could reach more than 820 nT.

Another aeromagnetic anomaly region is along the fault of Section 2, and the anomalies are closely related to the outcropped Carboniferous stratum that is mainly composed of basic volcanic rocks in a mid-oceanic-ridge volcanic environment, the Permian stratum that is composed of a set of clasolites with a few acids' volcanic intercalations, Carboniferous–Permian quartz diorite, and Cambrian gabbro and serpentinized peridotite. The magnetic intensity along this fault is between 100 nT and 300 nT. Forty-five samples are collected along Section 1 and Section 2 from the peridotites to measure their magnetism, and the magnetic susceptibility of these peridotite rocks could reach 4500 SI. Meanwhile, the regions in the southwest and north of the study area are covered by the Cretaceous stratum, which is a set of sandstones and conglomerates, and the Quaternary stratum, which is a set of migratory dunes and flood alluvial layers, are characteristic of low magnetism. The magnetic intensity in these regions is between −50 nT and −200 nT. Therefore, it is apparent that there is a magnetic interface in
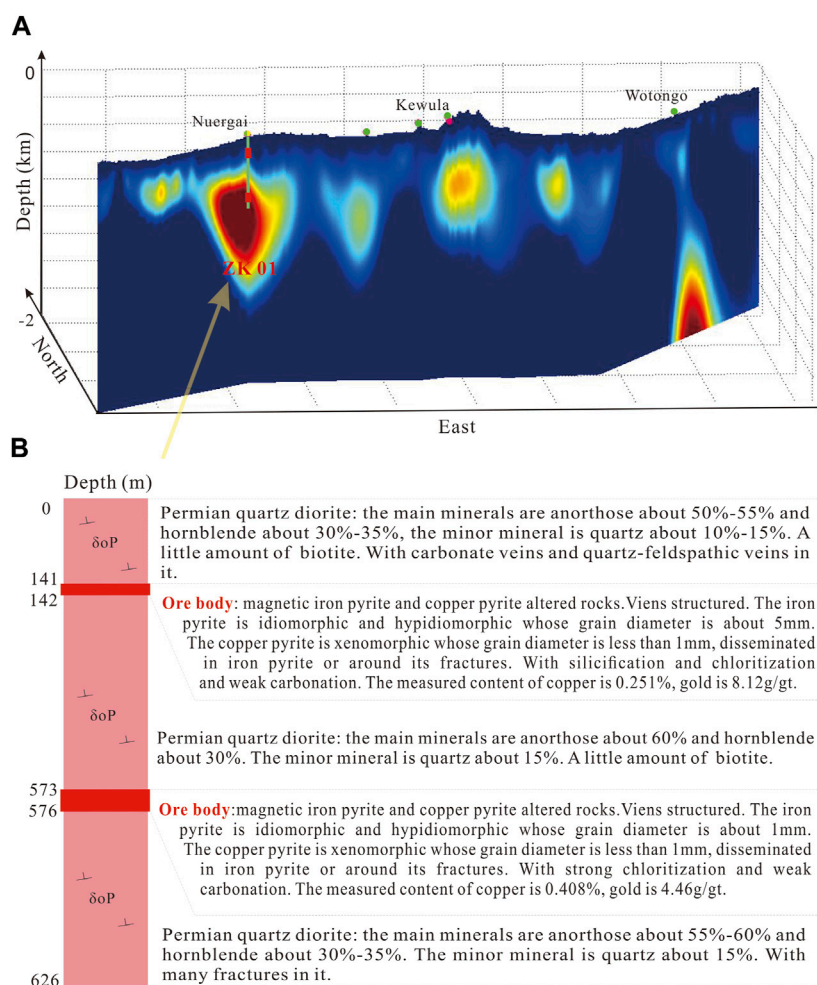
FIGURE 8
3D inversion result by MSVD–BEMD–MagFInv3D. **(A)** Inversed 3D cube of residual anomalies after denoising. **(B)** Mineral deposits and magnetic anomalies along the regional tectonic faults (or geological sections).

the deep region of the underground, and the high anomalies are mainly from the deep peridotite crystalline basement. It could also be inferred that the deep peridotite crystalline basement provided resources for the deposits listed in Table 1 in the study area, and these regional faults created a good environment for their formation. Most of the deposits along Section 1 are tectonic–hydrothermal-related, while the deposits along Section 2 are mainly tectonic-controlled. A tectonic–volcanogenic gold deposit in Asilen, a post-magmatic hydrothermal alteration-related gold deposit in Tebai, and a magmatic-liquated nickel deposit in Ekenrihan are located along Section 2. The structured fracture zones with mylonites could be commonly seen along Section 1 and Section 2, especially around the gold deposits. Both Section 3 and Section 4 partially pass through Section 1 and Section 2 to show regional geotectonic characteristics and verify the inversed deep magnetic anomalies. Some drilling holes are set on these deposits for the discovery of mineralization and the verification of deep magnetic anomalies.

3.2 Aeromagnetic denoising by MSVD

In this study, it is found that the value of aeromagnetic noise is often very low, which is usually concealed and hard to detect visually. However, it can be extracted by MSVD due to its sensitivity to weak noise. As is shown in Figure 6A of aeromagnetic noise detection by MSVD, the eigenvalues are automatically fitted into six straight lines by the weighted least square method in log–log coordination according to the turning points that can make the fitting errors of all lines reach minimum synchronously. Every straight line means some kind of noise or signal, of which the noise is reconstructed by the first and second lines, where the turning points are −7.23 and −0.84, as shown in Figure 6A. The detected noise by MSVD is visualized in Figures 6B,C. It is mainly fringe and random noise distributed in the south of the study area. The percent measured by the variance of such useless noise is just about 0.03%, but it induces the mode mixing problem, which has to be taken into consideration, especially when the percent of the fringe and random noise is
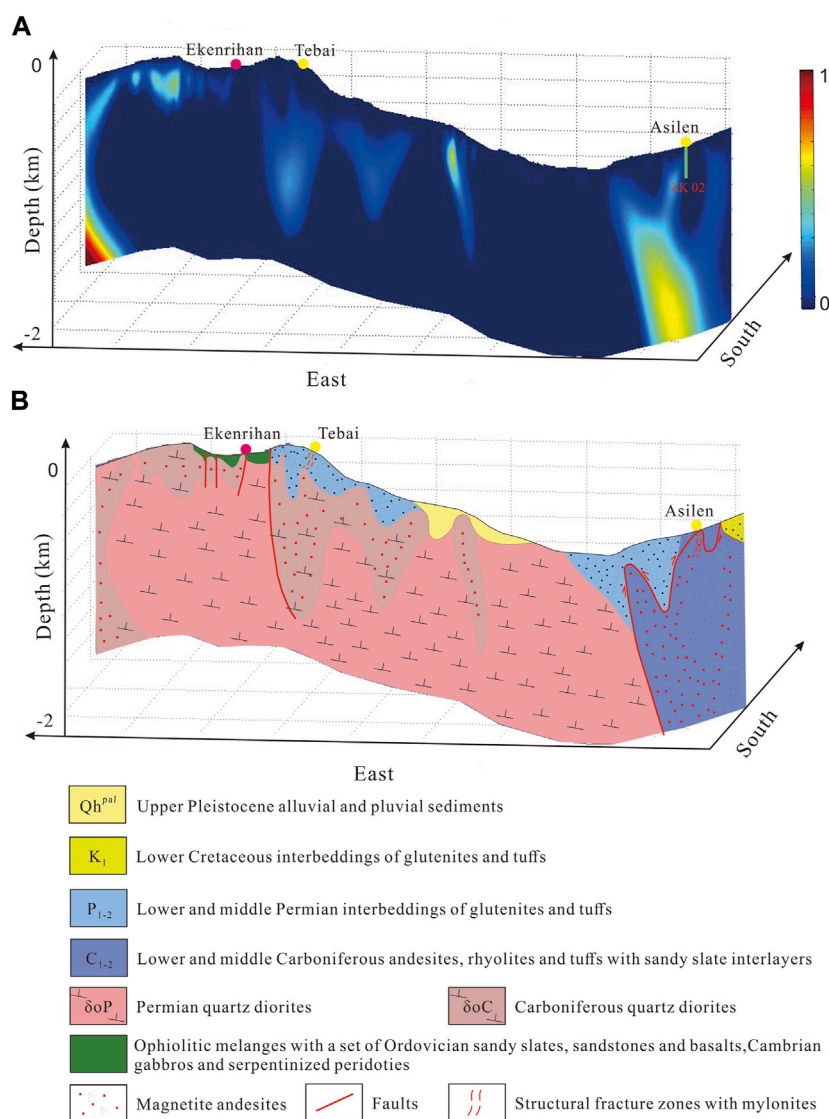
FIGURE 9
Section 1. **(A)** Section 1 from the inversed cube of 2 km depth by the proposed approach. **(B)** Detailed information of ZK 01 to verify the magnetic anomalies of the Au deposit in Nuergai.

high. In addition, it will also affect the accuracy of 3D inversion. Therefore, it is removed by subtracting it from the aeromagnetic data.

3.3 Residual anomalies extraction by improved BEMD

The parameter of SD and the termination condition of the error to measure colinearity is set as 0.3 and 0.0001, respectively. The decomposed results obtained by improved BEMD are shown in Figure 7, in which BIMF 1 in Figure 7A is a high-pass filter. The anomalies that are string–bead alike in BIMF 1 indicate the shallow–subsurface magnetism where regional faults and the tectonic–hydrothermal polymetallic deposits are often distributed along them. BIMF 2 in Figure 7B is a band-pass filter that shows the deeper or mantle-crustal anomalies, in which the deposits are distributed along two ore-prospecting directions. The first one is along the Asilen–Tebai reverse fault and is

associated with the subduction movement where the anomalies are induced by Carboniferous basic volcanic rocks of a mid-oceanic ridge and Carboniferous–Permian magnetic quartz diorites. The second one is along the Nuergai–Kewula–Wutongou reverse fault, which is strictly associated with tectonic–hydrothermal and contact-metasomatic deposits that were mainly formed between late Carboniferous and early Permian. There is also a famous big magnetite iron deposit named Kexiutata of skarn type on the east of this belt outside of this study area at a distance of about 10 km, which is within the intersection between Asilen–Tebai reverse fault and Nuergai–Kewula–Wutongou reverse fault, and was formed in the early Permian. Therefore, BIMF 1 and BIMF 2 are the local target anomalies we need. BIMF 3 in Figure 7C and Residue in Figure 7D are low-pass filters that show the deep mantle crystalline basement. The sum of BIMF 3 and Residue could be taken as regional anomalies to be subtracted from the denoised aeromagnetic data. Meanwhile, the residual anomalies could be extracted for 3D inversion.

FIGURE 10
Section 2. **(A)** Section 2 from the inversed cube of 2 km depth by the proposed approach. **(B)** Geological descriptions of section 2 by field investigation.

3.4 3D inversion by MagFInv3D

A wavenumber-domain iterative 3D imaging method with MagFInv3D is applied to inverse the local target magnetic anomalies for interpretation and mineral exploration. The parameter of iteration is set as five times, and the inversion depth is set as 10 km and 2 km to show the deep magnetic characteristics of different depths. The inversed 3D cube of the residual anomalies after MSVD denoising is shown in Figure 8A.

4 Validation and comparison

In order to show the relationship among regional tectonic structures, deposits, and targeted underground magnetic anomalies, four sections are sliced from the 3D inversion cube along the regional faults' directions (geological sections). The inversed cube is of the depth of 2 km and has 401 rows, 456 columns, and 200 layers. The geological sections and the mineral deposits along these regional faults are integrated by MATLAB 2022b and shown in Figure 8B, in which the deposits are strictly controlled by these regional faults.

There is a magnetic anomaly in Figure 9 of Section 1 where the Nuergai Cu–Au deposit is located and is of tectonic–hydrothermal genesis. It is verified by a drilling hole of ZK 01 that the underground rocks are mainly Permian quartz diorite that is composed of anorthose, hornblende, and quartz, with a little biotite. Two ore bodies were found within the depth between 141 m and 142 m and 573 m and
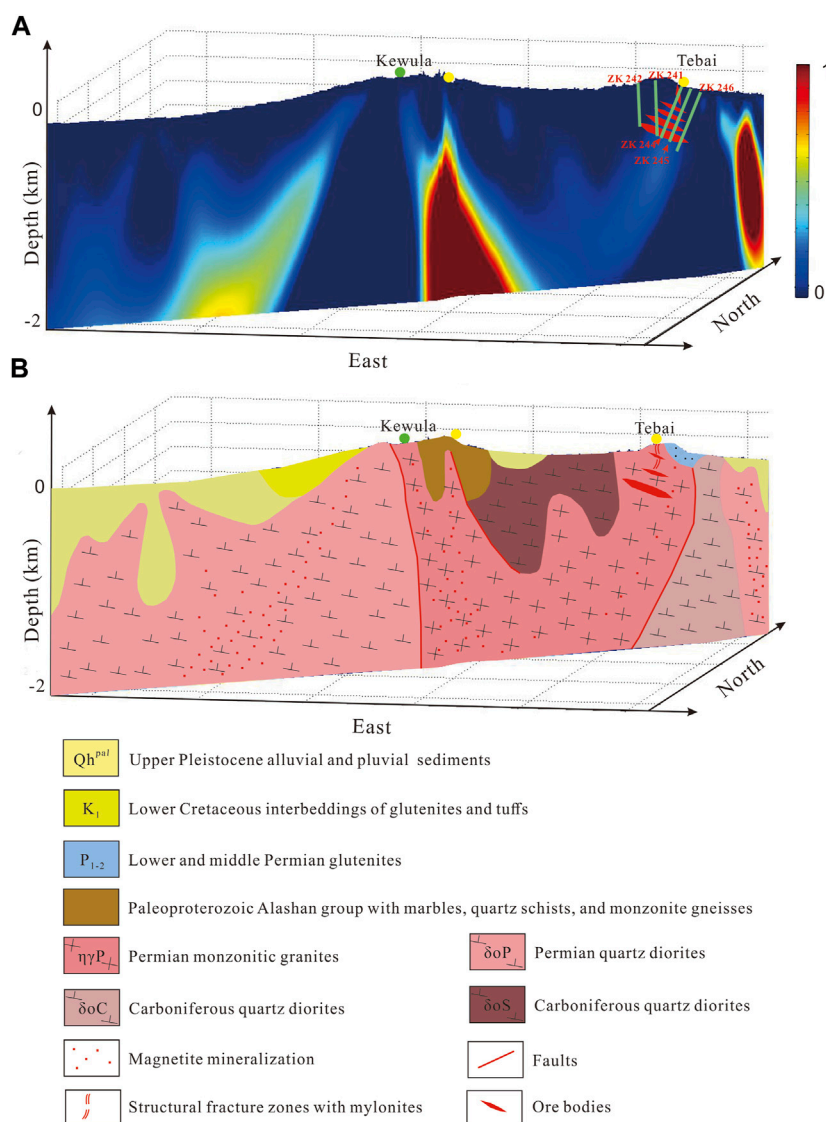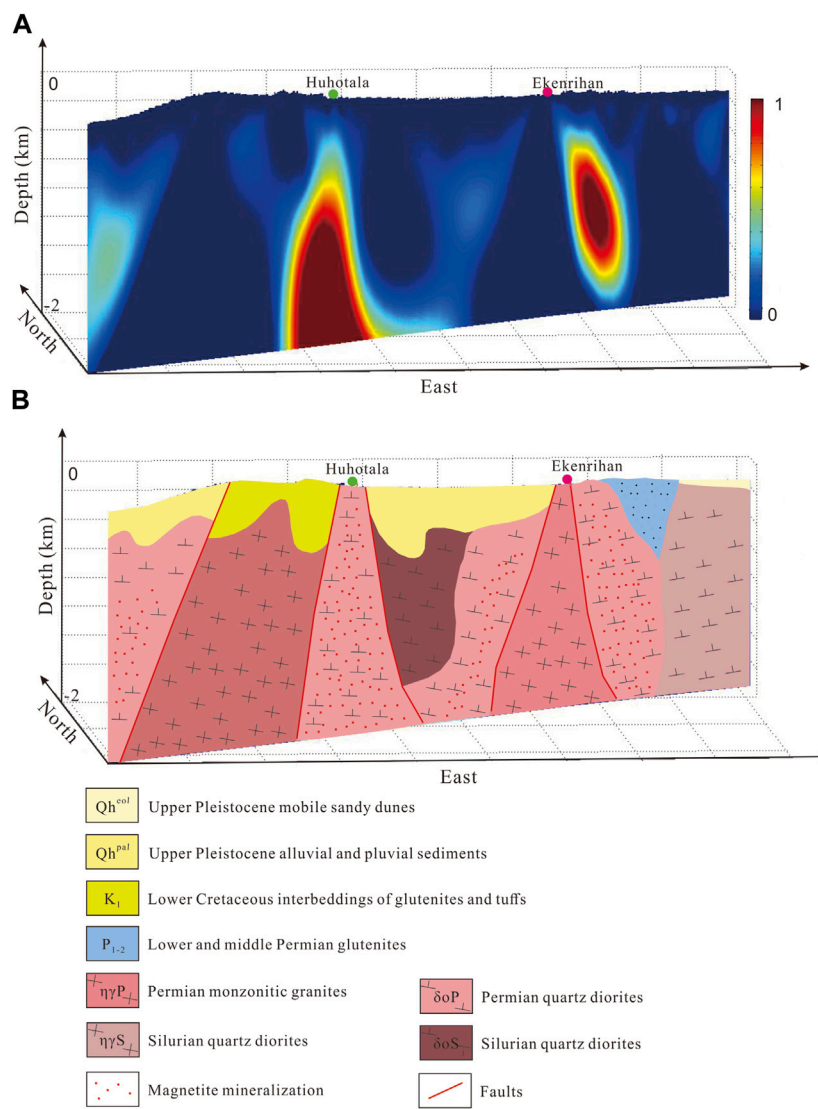
FIGURE 11
Section 3. **(A)** Section 3 from the inversed cube of 2 km depth by the proposed approach. **(B)** Geological descriptions of section 3 by field investigation.

576 m, respectively. The measured content of copper is 0.251% and 0.408%, and that of gold is 8.12 g/t and 4.46 g/t, respectively, in these two locations. In addition, both of them contained large amount of magnetic iron pyrite with copper pyrite disseminated around or in it, which corresponds to the high magnetic anomalies.

The high magnetic anomaly under the Asilen volcanogenic gold deposit along Section 2 in Figure 10 is verified by a drilling hole of ZK 02 of the depth of 355 m that it is induced by lower–middle Carboniferous volcanic andesites, rhyolites, and tuffs with sandy slate interlayers, which are enriched with structured fracture zones with mylonites. The measured Au, Ag, and Cu is 0.02%–0.04%, 0.70%–1.00%, and 0.0016%– 0.0086%, respectively, within the depth of 20 m–22 m,

30 m–31 m, 291 m–292 m, and 296 m–297 m. The high magnetic anomaly under the Tebai gold deposit, a famous medium-sized deposit that is on the intersection point between Section 2 in Figure 10 and Section 3 in Figure 11, is uncovered by drilling explorations of ZK 241, ZK 242, ZK 244, ZK 245, and ZK 246 that are exactly overlapped with the ore bodies. Structured fracture zones with mylonites could be seen on the ground surface and in the drilling holes, which created a good environment for the formation of the ore bodies, and the underground Carboniferous–Permian quartz diorites provided material resources for the ore bodies. It could be inferred by these drilling holes and field exploration that the high magnetic anomalies under Tebai and Ekenrihan are mainly induced by the Carboniferous quartz diorites and magnetic andesites.

FIGURE 12
Section 4. **(A)** Section 4 from the inversed cube of 2 km depth by the proposed approach. **(B)** Geological descriptions of section 4 by field investigation.

Meanwhile, the deposits around Kewula, Huhotala, and Ekenrihan are also controlled by the regional faults and are closely related to the underground magnetic anomalies induced by Permian monzonitic granite and quartz diorite in Figure 12 of Section 4.

Therefore, the inversed underground 3D magnetic anomalies could be taken as a sign of mineralization for targeting the deposits; further exploration could be conducted on the high-anomaly regions, especially around the known and verified deposits. The inversed result by the proposed approach of MSVD–BEMD–MagFInv3D in Figure 8 is compared with the one that is without removing the noise and regional anomalies in Figure 13. It could be seen that the local anomalies are more enhanced and embodied in the former. The magnetic anomalies emerge shallower to the surface after

removing the regional (background) anomalies, and more importantly, they are more exactly in accordance with the regional faults and the deposits. While the magnetic anomalies in the latter one, that is, without removing the noise and regional anomalies, are deeper underground, their shape and distribution of do not fit in properly with the regional faults and the known deposits, which are verified by field exploration of geological sections and delineated in Figures 9–12.

As for our future work, the inversed high-magnetic anomalies, especially around the known deposits and along the regional tectonic faults, should be explored further for finding more mineral deposits. The other denoising methods, regional–residual anomaly separation methods, and 3D inversion methods should be studied further with a comparison of the proposed approach and its effectiveness.
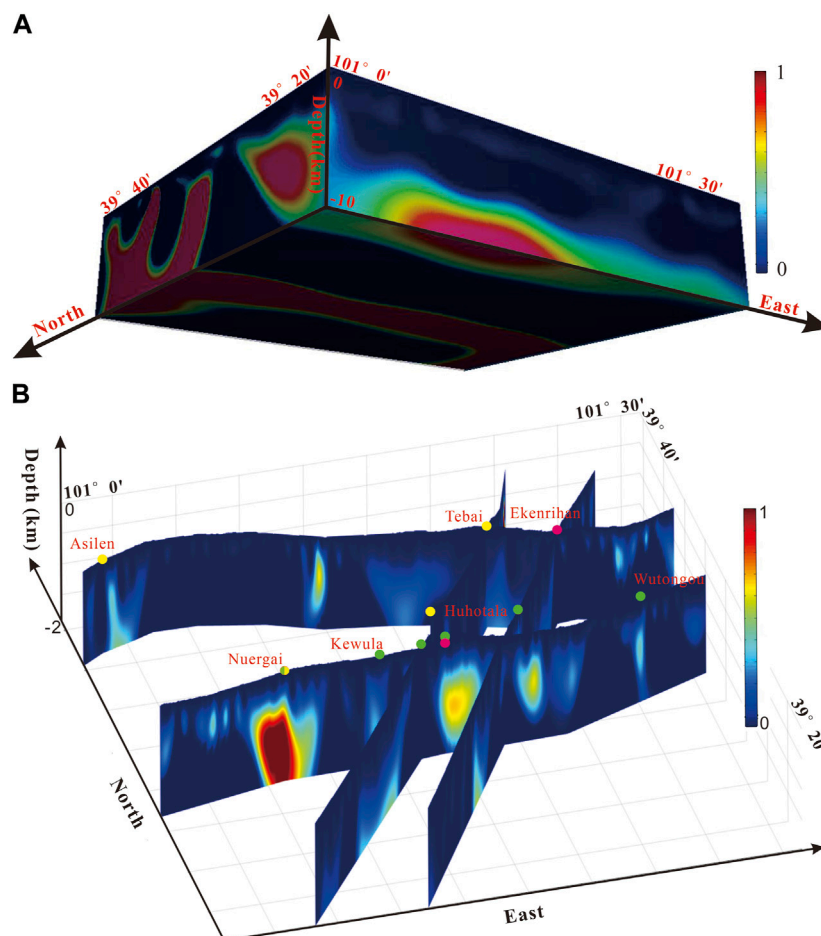
FIGURE 13
3D inversion result without removing the noise and regional anomalies. **(A)** Inversed 3D cube. **(B)** Mineral deposits and magnetic anomalies along the regional tectonic faults (or geological sections).

5 Conclusion

First, the pre-process of MSVD is efficient in aeromagnetic denoising. It could automatically detect the noise in it and effectively subtract it in this way. Thus, it could alleviate the mode mixing problem and improve the accuracy of 3D magnetic inversion.

Second, the improved BEMD is an effective method in separating local targeted anomalies from the regional background, data-driven and self-adaptive, orthogonal, and additive. As a dyadic self-adaptive filter bank, BIMF 1 is a high-pass filter applicable to interpreting the tectonic structures and is an indirect indicator to tectonic–hydrothermal-related polymetallic deposits. BIMF 2 is a band-pass filter applicable to prospecting metallogenic areas. BIMF 3+ residue is a low-pass filter and can be taken as regional anomalies. These filters are independent of one another, and residual anomalies could be extracted from them.

Third, the wavenumber–domain iterative approach for 3D imaging of magnetic anomalies and gradients with depth constraints is an effective and efficient way of dealing with magnetic 3D inversion. With the verification of four geological sections and some drilling holes, the genesis of the mineral deposits could be clearly revealed and more regional mineralization prospects could be delineated.

Generally speaking, the approach proposed by this study is an effective way of aeromagnetic denoising, residual anomaly extraction, and 3D inversion for mineral exploration. It is especially effective in exploring polymetallic deposits of high magnetism with tectonic and hydrothermal genesis.

Data availability statement

Author contributions

MM programmed the algorithm and wrote this paper. WZ, LX, and QG guided this research. YL, WW, and

HX drew some of the figures in the paper. All authors contributed to the article and approved the submitted version.

Funding

Acknowledgments

Conflict of interest

The authors declare that the research was conducted in the absence of any commercial or financial relationships that could be construed as a potential conflict of interest.

The reviewer LG declared a shared affiliation with the author MM to the handling editor at the time of review.

Publisher's note

All claims expressed in this article are solely those of the authors and do not necessarily represent those of their affiliated organizations, or those of the publisher, the editors, and the reviewers. Any product that may be evaluated in this article, or claim that may be made by its manufacturer, is not guaranteed or endorsed by the publisher.

References

Abdelrahman, E. M., and Sharafeldin, S. M. (1996). An iterative least-squares approach to depth determination from residual magnetic anomalies due to thin dikes. *J. Appl. Geophys.* 34, 213–220. doi:10.1016/0926-9851(95)00017-8

Al-Rahim, A. M. (2016). Separating the gravity field of Iraq by using bidimensional empirical mode decomposition technique. *Arabian J. Geosciences* 9 (1), 43–49. doi:10.1007/s12517-015-2118-7

Bencharef, M. H., Eldosouky, A. M., Zamzam, S., and Boubaya, D. (2022). Polymetallic mineralization prospectivity modelling using multi-geospatial data in logistic regression: The Diapiric Zone, Northeastern Algeria. *Geocarto Int.* 37 (27), 15392–15427. doi:10.1080/10106049.2022.2097481

Bouhrara, M., Maring, M. C., and Spencer, R. G. (2019). A simple and fast adaptive nonlocal multispectral filtering algorithm for efficient noise reduction in magnetic resonance imaging. *Magn. Reson. Imaging* 55, 133–139. doi:10.1016/j.mri.2018.08.011

Chen, Y., Zhang, L., and Zhao, B. (2019). Identification of the anomaly component using BEMD combined with PCA from element concentrations in the Tengchong tin belt, SW China. *Geosci. Front.* 10 (4), 1561–1576. doi:10.1016/j.gsf.2018.09.015

Cheng, Q. (2005). Multifractal distribution of eigenvalues and eigenvectors from 2D multiplicative cascade multifractal fields. *Math. Geol.* 37 (8), 915–927. doi:10.1007/s11004-005-9223-1

Cheng, Q., Xu, Y., and Grunsky, E. (2000). Integrated spatial and spectrum method for geochemical anomaly separation. *Nat. Resour. Res.* 9 (1), 43–52. doi:10.1023/A:1010109829861

Cui, Y., and Guo, L. (2019). A wavenumber-domain iterative approach for 3D imaging of magnetic anomalies and gradients with depth constraints. *J. Geophys. Eng.* 16 (6), 1032–1047. doi:10.1093/jge/gxz064

Di Pietro Paolo, D., Müller, H. P., Nolte, G., and Erné, S. N. (2006). Noise reduction in magnetocardiography by singular value decomposition and independent component analysis. *Med. Biol. Eng. Comput.* 44 (6), 489–499. doi:10.1007/s11517-006-0055-z

Ekpe, E. E., Ben, U. C., Ekwok, S. E., Ebong, E. D., Akpan, A. E., Eldosouky, A. M., et al. (2022). Assessment of natural radionuclide distribution pattern and radiological risk from rocks in precambrian oban massif, southeastern Nigeria. *Minerals* 12 (312), 1–19. doi:10.3390/min12030312

Eldosouky, A. M., El-qassas, R. A. Y., Pham, L. T., Abdelrahman, K., Alhumimidi, M. S., Bahrawy, A., et al. (2022). Mapping main structures and related mineralization of the arabian shield (Saudi arabia) using sharp edge detector of transformed gravity data. *Minerals* 12 (71), 71–20. doi:10.3390/min12010071

Eldosouky, A. M., El-Qassas, R. A. Y., Pour, A. B., Mohamed, H., and Sekandari, M. (2021). Integration of ASTER satellite imagery and 3D inversion of aeromagnetic data for deep mineral exploration. *Adv. Space Res.* 68 (9), 3641–3662. doi:10.1016/j.asr.2021.07.030

Eldosouky, A. M., Sehsah, H., Elkhateeb, S. O., and Pour, A. B. (2020). Integrating aeromagnetic data and Landsat-8 imagery for detection of post-accretionary shear zones controlling hydrothermal alterations: The Allaqi-Heiani Suture zone, South Eastern Desert, Egypt. *Adv. Space Res.* 65 (3), 1008–1024. doi:10.1016/j.asr.2019.10.030

ElGalladi, A., Araffa, S., Mekkawi, M., and Abd-AlHai, M. (2022). Exploring mineralization zones using remote sensing and aeromagnetic data, West Allaqi Area, Eastern-Desert, Egypt. *Egypt. J. Remote Sens. Space Sci.* 25 (2), 417–433. doi:10.1016/j.ejrs.2022.03.007

Elkhateeb, S. O., and Abdellatif, M. A. G. (2018). Delineation potential gold mineralization zones in a part of Central Eastern Desert, Egypt using Airborne Magnetic and Radiometric data. *NRIAG J. Astronomy Geophys.* 7 (2), 361–376. doi:10.1016/j.nrjag.2018.05.010

Gabtni, H., and Jallouli, C. (2017). Regional-residual separation of potential field: An example from Tunisia. *J. Appl. Geophys.* 137, 8–24. doi:10.1016/j.jappgeo.2016.12.011

Gao, Y., Zhang, Z., Xiong, Y., and Zuo, R. (2016). Mapping mineral prospectivity for Cu polymetallic mineralization in southwest Fujian Province, China. *Ore Geol. Rev.* 75, 16–28. doi:10.1016/j.oregeorev.2015.12.005

Guo, L., Meng, X., Chen, Z., Li, S., and Zheng, Y. (2013). Preferential filtering for gravity anomaly separation. *Comput. Geosciences* 51, 247–254. doi:10.1016/j.cageo.2012.09.012

Gupta, V. K., and Ramani, N. (1980). Some aspects of regional-residual separation of gravity anomalies in a precambrian terrain. *Geophysics* 45 (9), 1412–1426. doi:10.1190/1.1441130

Hou, W., Yang, Z., Zhou, Y., Zhang, L., and Wu, W. (2012). Extracting magnetic anomalies based on an improved BEMD method: A case study in the pangxidong area, south China. *Comput. Geosciences* 48, 1–8. doi:10.1016/j.cageo.2012.05.006

Huang, J., Zhao, B., Chen, Y., and Zhao, P. (2010). Bidimensional empirical mode decomposition (BEMD) for extraction of gravity anomalies associated with gold mineralization in the Tongshi gold field, Western Shandong Uplifted Block, Eastern China. *Comput. Geosciences* 36 (7), 987–995. doi:10.1016/j.cageo.2009.12.007

Innocent, A. J., Chidubem, E. O., and Chibuzor, N. A. (2019). Analysis of aeromagnetic anomalies and structural lineaments for mineral and hydrocarbon exploration in Ikom and its environs southeastern Nigeria. *J. Afr. Earth Sci.* 151, 274–285. doi:10.1016/j.jafrearsci.2018.12.011

Keating, P., and Pinet, N. (2011). Use of non-linear filtering for the regional-residual separation of potential field data. *J. Appl. Geophys.* 73 (4), 315–322. doi:10.1016/j.jappgeo.2011.02.002

Kharbish, S., Eldosouky, A. M., and Amer, O. (2022). Integrating mineralogy, geochemistry and aeromagnetic data for detecting Fe–Ti ore deposits bearing layered mafic intrusion, Akab El-Negum, Eastern Desert, Egypt. *Sci. Rep.* 12 (15474), 15474–15519. doi:10.1038/s41598-022-19760-x

Lee, S., and Lee, Y. (2021). Performance evaluation of median-modified Wiener filter algorithm in high-resolution complementary metal–oxide–semiconductor radio-magnetic X-ray imaging system: An experimental study. *Nucl. Instrum. Methods Phys. Res. Sect. A Accel. Spectrom. Detect. Assoc. Equip.* 1010 (165509), 165509–165516. doi:10.1016/j.nima.2021.165509

Li, Y., and Nabighian, M. (2015). "Tools and techniques: Magnetic methods of exploration - principles and algorithms," in *Treatise on geophysics* (Berlin, Germany: Springer), 11. doi:10.1016/B978-0-444-53802-4.00196-2

Lin, T., Yu, S., Zhao, H., Zhang, Y., and Sun, H. (2022). Harmonic noise cancellation of magnetic resonance sounding signal based on wavelet modulus maximum. *J. Appl. Geophys.* 207 (104839), 104839–9. doi:10.1016/j.jappgeo.2022.104839

Little, A. V., Maggioni, M., and Rosasco, L. (2017). Multiscale geometric methods for data sets I: Multiscale SVD, noise and curvature. *Appl. Comput. Harmon. Analysis* 43, 504–567. doi:10.1016/j.acha.2015.09.009

Liu, B., Sang, X., Xing, S., and Wang, B. (2015). Noise suppression in brain magnetic resonance imaging based on non-local means filter and fuzzy cluster. *Optik* 126 (21), 2955–2959. doi:10.1016/j.ijleo.2015.07.056

Ma, M., Wang, C. H., Li, X., Gao, Q., Gong, W. G., and Shi, S. X. (2019). Aeromagnetic anomalies interpretation based on improved bi-dimensional empirical mode decomposition (BEMD) and RGB composition. *IOP Conf. Ser. Earth Environmental Sci.* 237 (5), 052002–052011. doi:10.1088/1755-1315/237/5/052002

Mahdi, A. M., Eldosouky, A. M., el Khateeb, S. O., Youssef, A. M., and Saad, A. A. (2022). Integration of remote sensing and geophysical data for the extraction of hydrothermal alteration zones and lineaments; Gabal Shilman basement area, Southeastern Desert, Egypt. *J. Afr. Earth Sci.* 194 (104640), 104640–104711. doi:10.1016/j.jafrearsci.2022.104640

Mamouch, Y., Attou, A., Miftah, A., Ouchchen, M., Dadi, B., Moussaid, A., et al. (2023). Aeromagnetic data of the kelâat M'gouna inlier (jbel saghro, eastern anti-atlas, Morocco): Geotectonic and mining implications. *J. Afr. Earth Sci.* 197 (104744), 104744–104812. doi:10.1016/j.jafrearsci.2022.104744

Mandal, A., and Niyogi, S. (2018). Filter assisted bi-dimensional empirical mode decomposition: A hybrid approach for regional-residual separation of gravity anomaly. *J. Appl. Geophys.* 159, 218–227. doi:10.1016/j.jappgeo.2018.09.003

Martínez-Moreno, F. J., Galindo-Zaldívar, J., Pedrera, A., Teixidó, T., Peña, J. A., and González-Castillo, L. (2015). Regional and residual anomaly separation in microgravity maps for cave detection: The case study of Gruta de las Maravillas (SW Spain). *J. Appl. Geophys.* 114, 1–11. doi:10.1016/j.jappgeo.2015.01.001

Muundjua, M., Hart, R. J., Gilder, S. A., Carporzen, L., and Galdeano, A. (2007). Magnetic imaging of the Vredefort impact crater, South Africa. *Earth Planet. Sci. Lett.* 261, 456–468. doi:10.1016/j.epsl.2007.07.044

Ortiz-Alemán, C., and Urrutia-Fucugauchi, J. (2010). Aeromagnetic anomaly modeling of central zone structure and magnetic sources in the Chicxulub crater. *Phys. Earth Planet. Interiors* 179, 127–138. doi:10.1016/j.pepi.2010.01.007

Saada, S. A., Eldosouky, A. M., Kamel, M., Khadragy, A., Abdelrahman, K., Fnais, M. S., et al. (2022). Understanding the structural framework controlling the sedimentary basins from the integration of gravity and magnetic data: A case study from the east of the qattara depression area, Egypt. *J. King Saud Univ. - Sci.* 34 (101808), 101808–101812. doi:10.1016/j.jksus.2021.101808

Shebl, A., Abdellatif, M., Elkhateeb, S. O., and Csámer, Á. (2021). Multisource data analysis for gold potentiality mapping of atalla area and its environs, central eastern desert, Egypt. *Minerals* 11 (641), 641–719. doi:10.3390/min11060641

Spector, A., and Grant, F. S. (1970). Statistical models for interpreting aeromagnetic data. *Geophysics* 35 (2), 293–302. doi:10.1190/1.1440092

Sridhar, M., Markandeyulu, A., Chawla, A. S., and Chaturvedi, A. K. (2018). Analyses of aeromagnetic data to delineate basement structures and reveal buried igneous bodies in kaladgi basin, Karnataka. *J. Geol. Soc. India* 91 (2), 165–173. doi:10.1007/s12594-018-0830-0

Tazi, M. J., Azzab, D. el, Charroud, M., Jabrane, O., Ouahzizi, Y., Zahour, R., et al. (2022). Identification of potential mineral exploration targets from the interpretation of aeromagnetic data covering the Sirwa region (Central Anti-Atlas, Morocco). *Sci. Afr.* 17 (01351), 013511–e1413. doi:10.1016/j.sciaf.2022.e01351

Wang, G., Zhang, S., Yan, C., Xu, G., Ma, M., Li, K., et al. (2012). Application of the multifractal singular value decomposition for delineating geophysical anomalies associated with molybdenum occurrences in the Luanchuan ore field (China). *J. Appl. Geophys.* 86, 109–119. doi:10.1016/j.jappgeo.2012.07.013

Xiong, S. (2021). Research achievements of the Qinghai-Tibet Plateau based on 60 years of aeromagnetic surveys. *China Geol.* 4 (1), 1–31. doi:10.31035/cg2021029

Xu, G., Cheng, Q., Zuo, R., and Wang, H. (2016). Application of improved bi-dimensional empirical mode decomposition (BEMD) based on Perona-Malik to identify copper anomaly association in the southwestern Fujian (China). *J. Geochem. Explor.* 164, 65–74. doi:10.1016/j.gexplo.2015.09.013

Zahra, H. S., and Nakhla, A. M. (2016). Tectonic and structural setting of the northeastern central Gulf of Suez area using aeromagnetic data. *J. Afr. Earth Sci.* 115, 1–16. doi:10.1016/j.jafrearsci.2015.12.012

Zhang, Z., Wang, G., Ma, Z., Carranza, E. J. M., Jia, W., Du, J., et al. (2020). Batholith-stock scale exploration targeting based on multi-source geological and geophysical datasets in the Luanchuan Mo polymetallic district, China. *Ore Geol. Rev.* 118 (103225), 103225–103320. doi:10.1016/j.oregeorev.2019.103225

Zhao, B. B., and Chen, Y. Q. (2011). Singular value decomposition (SVD) for extraction of gravity anomaly associated with gold mineralization in Tongshi gold field, Western Shandong Uplifted Block, Eastern China. *Nonlinear Process. Geophys.* 18 (1), 103–109. doi:10.5194/npg-18-103-2011

Zhao, J., Zhao, P., and Chen, Y. (2016). Using an improved BEMD method to analyse the characteristic scale of aeromagnetic data in the Gejiu region of Yunnan, China. *Comput. Geosciences* 88, 132–141. doi:10.1016/j.cageo.2015.12.016

Zhu, X., and Lu, M. (2021). Fault structures and magmatic intrusions inferred from magnetic data for the Southern Great Xing'an Range, northern China. *Ore Geol. Rev.* 135 (104206), 104206–104216. doi:10.1016/j.oregeorev.2021.104206

Zhu, X., Wang, T., Huang, H., and Zheng, H. (2022). An aeromagnetic study of fault structures underneath the region across the Chinese Altai orogen, Junggar Basin, Tianshan orogen, and Tarim Basin. *J. Asian Earth Sci.* 239 (105418), 105418–105514. doi:10.1016/j.jseaes.2022.105418